High-Order Commensurate Zwitterionic Quinonoid Phase Induces a Nanoscale Dipole Lattice on Graphene

Gaelle Nassar, Diego Cortés-Arriagada, Luis Sanhueza-Vega, Périne Landois, Matthieu Paillet, Haitham Hrich, Sylvie Contreras, Olivier Siri, Simon Pascal, Laurence Masson, et al.

High-Order Commensurate Zwitterionic Quinonoid phase induces a Nanoscale Dipole lattice on Graphene.

*Gaëlle Nassar[1], Diego Cortes-Arriagada[2], Luis Sanhueza-Vega[3-4], Périne Landois[5], Matthieu Paillet[5], Haitham Hrich[5], Sylvie Contreras[5], Olivier Siri[1], Simon Pascal[1], Laurence Masson[1], Conrad Becker[1], Alain Ranguis[1], Romain Parret[1], Gabriel Canard[1] and Thomas Leoni[1]**

[1]Aix Marseille Université, CNRS, CINaM, UMR 7325, Campus de Luminy, 13288 Marseille, France.

[2]Programa Institucional de Fomento a la Investigación, Desarrollo e Innovación, Universidad Tecnológica Metropolitana, Ignacio Valdivieso 2409, San Joaquín, Santiago, 8940577, Chile.

[3]Departamento de Ciencias Biológicas y Químicas, Facultad de Recursos Naturales, Universidad Católica de Temuco, Temuco, Chile.

[4]Núcleo de Investigatión en Bioproductos y Materiales Avanzados (BioMA), Universidad Católica de Temuco, Av. Rudecindo Ortega, 02950, Temuco, Chile.

[5]Laboratoire Charles Coulomb, UMR 5221, CNRS Université de Montpellier, Place Eugène Bataillon, 34095, Montpellier, France.

ABSTRACT

Since the introduction of hybrid van der Waals Heterostructures (h-vdWH) for device architecture development, many vertically staked organic two-dimensional (2D) materials have been investigated in order to control transport properties. This article introduces a novel h-vdWH that achieves periodic interaction by the development of a superlattice. We describe a complete investigation of the di-phenyl functionalized *p*-benzoquinonemonoimine zwitterion (DPQZ) on Highly Oriented Pyrolytic Graphite (HOPG) and monolayer graphene using high-resolution Scanning Tunneling Microscopy (STM) images and numerical simulations. The molecular phase on both substrates exhibits a structurally identical anti-parallel dipole alignment in a head-to-tail dimer configuration. Density Functional Theory (DFT) calculations reveal that this molecular adsorption induces a local dipole at the graphene interface due to the rearrangement of electron density distribution.

Introduction

The study of supramolecular networks on 2D materials, known as hybrid van der Waals (h-vdWH) Heterostructures,[1] is an emerging topic due to its pivotal role in tailoring materials properties at the nanoscale, resulting in the synthesis of various device architectures based on p-n heterojunction, such as antiambipolar transistors,[2] barristors[3] or field effect transistors based on charge transfer from the organic electronic resonant state to the conduction band of the substrate.[4,5] Beyond these global effects on transport properties in transistor-like configurations, the precise control of the position of individual molecules, resulting from the crystalline order of the supramolecular network, can lead to specific, periodic molecule-substrate interactions. Due to their extreme surface sensitivity, the electrical characteristics of 2D materials can be strongly modified by a weak perturbation such as a physisorbed molecule. And the combination of these two effects, i) a strong influence arising from a weak perturbation and ii) a spatially periodic perturbation, should have a significant impact on the band structure of the h-vdWH.[6]

This topic has gained interest since the experimental demonstration of the existence of a flat band induced by moiré effect in twisted bilayer graphene.[7] Staking two sheets of two-dimensional (2D) materials having vdW interactions, either with different lattice parameters or with an identical lattice parameter but rotated by some angle relative to each other, induces a periodically modulated surface potential related to the resultant superlattice moiré pattern. An intricate interplay between the moiré and interlayer hybridization effects occurs on these systems, and under specific conditions, can lead to a flattening of a portion of the band structure and finally to the formation of strongly correlated electronic systems.[8] The concept of these heterostructures is versatile enough to envision the replacement of one inorganic layer by a 2D supramolecular layer of dipolar molecules. These new h-vdWH systems meet two of the requirements for the emergence of

strongly correlated electronic systems: first, a van der Waals interaction between graphene and the 2D layer, and second, the formation of a periodic modulation of the surface potential. Indeed, a physisorbed molecule with an intrinsic permanent dipole moment generates an electric field that disturbs the electronic density of the substrate in the local region underneath the molecule, modifying the local surface potential. The growth of supramolecular networks of dipolar molecules adsorbed on graphene should therefore periodically modulate the surface potential due to the order of the network. First attempts to achieve this modulation have been performed on graphene and HOPG surfaces in liquid environment.[9] These results showed that it is possible to obtain a periodic modulation of the potential of the order of 0.8 V in one dimension, and to exploit a subtle photo-induced change in the chemical structure of the starting molecule to modify the amplitude of this potential. Moreover, in most cases, the same molecular lattice is formed on HOPG and graphene, indicating that HOPG can be used as a model surface for the structural study of organic networks on graphene.[10–13]

p-benzoquinonemonoimine zwitterions (DPQZ) are among the molecules with the strongest permanent internal dipole (10 Debyes) and appear to be ideal candidates for achieving a modulation of the surface potential. Surface adsorption of some derivatives of zwitterionic quinones has been studied [14] and revealed supramolecular networks on metallic[15] and HOPG substrates,[16] with various adsorption geometries (flat lying or normal adsorption). One of the main findings of these studies is that, depending on the adsorption geometry, the supramolecular network arrangement, the substrate interaction, the interface dipole can be changed by a variety of effects such as charge transfer, mirror dipoles, and surface-enhanced dipole moments. Moreover, the resulting pattern of the dipole network is not simply related to the superposition of these two of properties: the dipole orientation of a single molecule and the supramolecular arrangement. The

interplay between multiple interactions (Coulomb forces, details of the local electrostatic potential and intermolecular interactions) leaves the resulting pattern *a priori* unpredictable without measurements or simulation.

In this article, we present a complete investigation of the supramolecular growth of a *p*-benzoquinonemonoimine zwitterionic derivative (Scheme 1) on surfaces of HOPG and a graphene monolayer grown on 4H-SiC(0001). The molecular dipoles considered here are in-plane rather than out-of-plane, like in SAMs. The experimental study using scanning tunneling microcopy (STM) is complemented by a multilevel computational model of the self-assembly on graphene and its resulting dipole in a local domain. The experimental setup takes place in a ultrahigh vacuum (UHV) environment by STM. We demonstrate that under specific growth parameters, these molecules can self-assemble into a single phase with a stable crystallographic order over several microns. Using a dedicated data analysis method based on auto-correlation, we extract the interfacial correlation matrix of this supramolecular network, which highlights the presence of a highly-ordered Commensurate (HOC) phase with HOPG and graphene. These experiments, supported by calculations, explain the origin of the stability of the organic layer in terms of intermolecular and molecule-substrate interactions. Moreover, simulations of the resulting dipole on local domains are performed to evaluate its magnitude.

Experimental and Theoretical Methods

1.1. Organic Synthesis

The molecule used in this study, Di-Phenyl substituted *p*-benzoquinonemonoimine Zwitterion (DPQZ), was synthesized and purified according to established procedures.[17,18] It

consists in performing a transamination reaction on the quinonoid ring of the parent zwitterion QZ (Scheme 1).

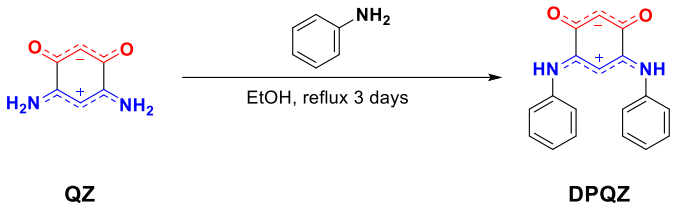

Scheme 1. Synthetic route of the Di-Phenyl functionalized zwitterion DPQZ.[17,18] These structures are 12π-electron zwitterionic quinones with a delocalization present on two independent subunits of the molecule: the positive charge is localized between the nitrogen atoms and the negative charge is localized between the oxygen atoms.

1.2. Experimental Methods

All STM experiments and sample preparations were performed under UHV conditions using a commercial low-temperature STM with pressures in the 10^{-11} mbar range. The HOPG surface was prepared by scotch tape mechanical cleaving, followed by annealing at 400 °C for 1 h under UHV. The DPQZ molecules were deposited with high reproducibility by thermal sublimation from a molecular Kentax evaporator with the quartz crucible held at 135 °C. The coverage rate of the surface by the molecules was estimated via the acquisition of STM images. Several depositions of molecules with different sublimation times but constant quartz crucible and substrate temperatures were carried out and then analyzed by STM image. These analyzes made it possible to estimate the sublimation times corresponding to approximately one monolayer. One monolayer of these molecules was deposited on a HOPG (0001) surface at room temperature after 8 min of exposure under UHV in the 10^{-10} mbar range during the deposition. The sample was then transferred into the analysis chamber and cooled down to liquid nitrogen temperature (≃78 K). The graphene surface was synthesized *via* 4H-SiC (0001) sublimation at low argon pressure.[19,20] Once introduced

in the UHV chamber it was annealing at 400 °C for 1 h before deposition. 1 ML of DPQZ molecules was deposited after 8 min exposure under UHV on a graphene on the 4H-SiC(0001) surface cooled to roughly -140 °C.

The cleanliness and structural quality of the substrates was checked by STM prior to any deposition. The STM images were obtained in constant current mode at the liquid nitrogen temperature for both the sample and the electrochemical etched tungsten tips. The free software package Gwyddion was used for the analysis of the STM images.[21] All STM images presented are raw acquired data except for standard plane subtraction and one-dimensional Fast Fourier Transform (1D-FFT) filtering at 150 Hz along the horizontal direction.

1.3. Computational Methods

The graphene monolayer was derived from a pristine graphite crystal structure, with optimized C-C bond lengths of 1.42 Å. The unit cell was extended up to contain more than ~1300 carbon atoms, and it was converted to a non-periodic structure where dangling bond at the edges were completed with hydrogen atoms. Then, this model was used to adsorb different DPQZ stacked patterns. The most stable graphene-DPQZ stacked patterns were found by predicting all possible packing arrangements in the Polymorph module of Material Studio 2022 and using the Dreiding force field.[22] The initial adsorption patterns onto graphene were obtained by Metropolis Monte Carlo search in the Adsorption Locator module in combination with the Dreiding force field. Further geometry optimizations of all the 2D self-assembled structures were performed with the GFN-FF method in the ORCA 5.0 code; energies of the optimized systems with ~2000 atoms were recomputed with the extended semi empirical tight-binding model GFN2-xTB.[23] In addition, Density Functional Theory (DFT) calculations were performed on selected structures using the generalized gradient approximation (GGA) PBE functional combined with the all-electron def2-

SVP basis sets and DFT-D3BJ dispersion correction.[24–27] Binding energies (E_{bind}) were further decomposed by the energy decomposition analysis based on absolutely localized molecular orbitals (ALMO-EDA)[28,29]: $-E_{bind}=\Delta E_{charge\text{-}transfer}+\Delta E_{polarization}+\Delta E_{electrostatics}+\Delta E_{dispersion}+\Delta E_{Pauli}$, where ΔE_i terms stand for the energy lowering due to charge transfer, polarization, intermolecular electrostatics, and dispersion forces, respectively; ΔE_{Pauli} account for the Pauli repulsion energy. DFT calculations were performed in the ORCA 5.0 and QCHEM 5.4 codes.[30,31] Non-covalent interactions were studied with the Independent Gradient Model (IGM),[32] where the δg^{inter} index uniquely defines intermolecular interaction regions: $|\delta g^{inter}|=|\nabla\rho^{GM,inter}|-|\nabla\rho|$, where $\nabla\rho$ stands for the electron density gradient, and $\nabla\rho^{IGM,inter}$ is an upper limit to $\nabla\rho$. Electron-density-based analyses were performed in the Multiwfn 3.8 program.[33] Further details on the computational methodology are included in the supporting information.

Results and Discussion

1. Scanning Tunneling Microscopy

1.1. DPQZ assembly on HOPG

The constant current STM image in Figure 1a shows the extended molecular phase with a single orientation after the deposition of DPQZ molecules on HOPG surface. The bright or dark large-scale bent bands visible below the surface are dislocations or stacking defaults on the HOPG surface attributed to the stacking of HOPG sheets. Considering only the molecular layer, this image displays a single phase extended on over more than 400 nm in diameter. This phase comprises multiple domains, all of which have the same orientation (Figure 1b). The domain boundaries are marked with red arrows on Figure 1b. The domains exhibit anisotropic growth behavior with almost uninterrupted growth (several micrometer) in the direction of the red arrows. On the

contrary, in the direction of the white lines, their size varies from ~9 nm to several tens of nanometers. This anisotropic behavior is discussed further below. In addition to domain walls, periodic lines of brighter contrast can be distinguished and are highlighted by white lines in Figures 1b-c.

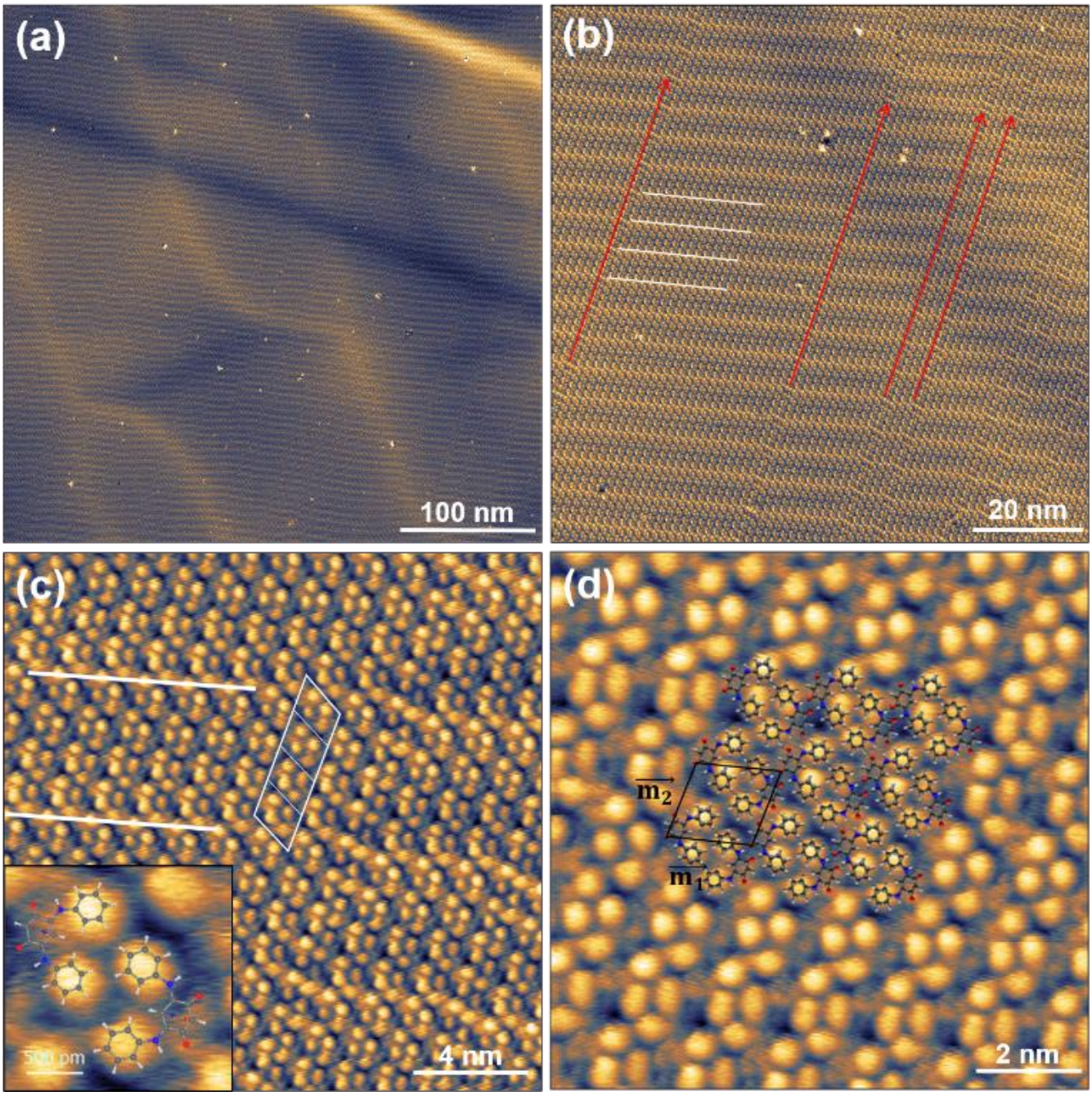

Figure 1. STM images of the same area of DPQZ molecules adsorbed on a HOPG surface at different scales. The images were recorded at a tunneling current of I_t= 2 pA and a sample voltage of V_s= 1.0 V. (a) Large scale image showing the extended molecular phase with the a single orientation. (b) Domain boundaries highlighted with red arrows and moiré effects are observed on

the surface are highlighted by white lines. (c) The predominant molecular motif is highlighted by a white parallelogram (d) The proposed molecular-scale model.

Between two lines of brighter contrast, one can distinguish four identical, periodic motifs highlighted by a white parallelogram (Figure 1c). Each motif consists of four bright features and two dark features (see inset of Figure 1c). Given the size and angles of the molecules, we attribute the bright features to the aromatic cores and the darker features to the quinonoid cores of two DPQZ molecules. Other high-resolution images confirmed this pattern (Figure S1). According to this adsorption geometry, the DPQZ self-assemble in a head-to-tail configuration with their dipole moment aligned along $\mathbf{m_1}$. This assembly geometry seems to be guided by NH···O hydrogen bonds following a similar intermolecular interaction reported for zwitterionic quinonemonoimines.[14–16,34–37]

It is important to note that the origin of the periodic bright lines along $\mathbf{m_1}$, which leads to a moiré pattern, could be a consequence of the lattice mismatch between the molecular network and the HOPG network. To explore this hypothesis, we establish the epitaxial relationship between these two networks. True epitaxy implies congruence of adsorbate and substrate lattices at the unit cell level. However, very often, these strict conditions are not met, and one possible alternative is the formation of a HOC superstructure that can be accompanied by a moiré pattern. Commensurate moiré patterns can be viewed as actual superstructures and are described by a unit cell with lattice parameters and a lattice defined through base translation vectors that we will name $\mathbf{a_{moiré}}$ and $\mathbf{b_{moiré}}$.[38] These base translation vectors as well as the molecular lattice translation vectors $\mathbf{m_1}$ and $\mathbf{m_2}$ are associated to the substrate lattice translation vectors $\mathbf{g_1}$ and $\mathbf{g_2}$ by the following relationships:

$$\begin{pmatrix} a_{moiré} \\ b_{moiré} \end{pmatrix} = \begin{pmatrix} a_{1,1} & a_{1,2} \\ a_{2,1} & a_{2,2} \end{pmatrix} \begin{pmatrix} g_1 \\ g_2 \end{pmatrix} \quad (1)$$

$$\begin{pmatrix} m_1 \\ m_2 \end{pmatrix} = \begin{pmatrix} b_{1,1} & b_{1,2} \\ b_{2,1} & b_{2,2} \end{pmatrix} \begin{pmatrix} g_1 \\ g_2 \end{pmatrix} \quad (2)$$

If the correlation matrix in eq. 1 contains only integer values the superstructure originating from the molecular lattice and HOPG lattice mismatch can be qualified as being of HOC type. To get the interfacial lattice correlation on HOPG, the identification of diffraction spots using Low Energy Electron Diffraction (LEED) patterns becomes challenging due to the bending of carbon flakes on the surface.

We could compare both structures in real space with atomic resolution by using two high-resolution STM images of these networks. However, at the liquid nitrogen temperature, there is distortion of images caused by the thermal drift and creep of the piezo-electric scanner. These distortions are of a nonlinear character and their compensation involves the application of corrections on the vectors' lengths and angles. The error bars on these quantities, which we estimated by comparing images of the HOPG lattice and the molecular lattice acquired separately, lead to error bars>1 on the correlation matrix coefficients. This prevents us from ensuring the strictly integer character of the coefficients of the correlation matrix, the true epitaxy relationship, and therefore the presence of a commensurate molecular phase. To avoid this, we can compare the two lattices in the same STM image. Thus, we deposited less than a monolayer of DPQZ molecules on the HOPG substrate and imaged at the interface between the organic layer and HOPG by STM (Figure 2a).

In Figure 2a, the molecular layer has a poor resolution because we adjusted the tunneling parameters to obtain atomic resolution on HOPG, which are not suitable to image the molecular layer that possesses a higher tunneling barrier than HOPG. Nevertheless, we can perceive the same molecular phase as the one observed at the monolayer, which is made up of contrasting lines separated by four identical recurrent molecular motifs (see Figure S2). This poor resolution prevents us from directly acquiring the lattice parameters of the molecular layer; however, the information of the periodic character of the network is preserved and can be extracted.

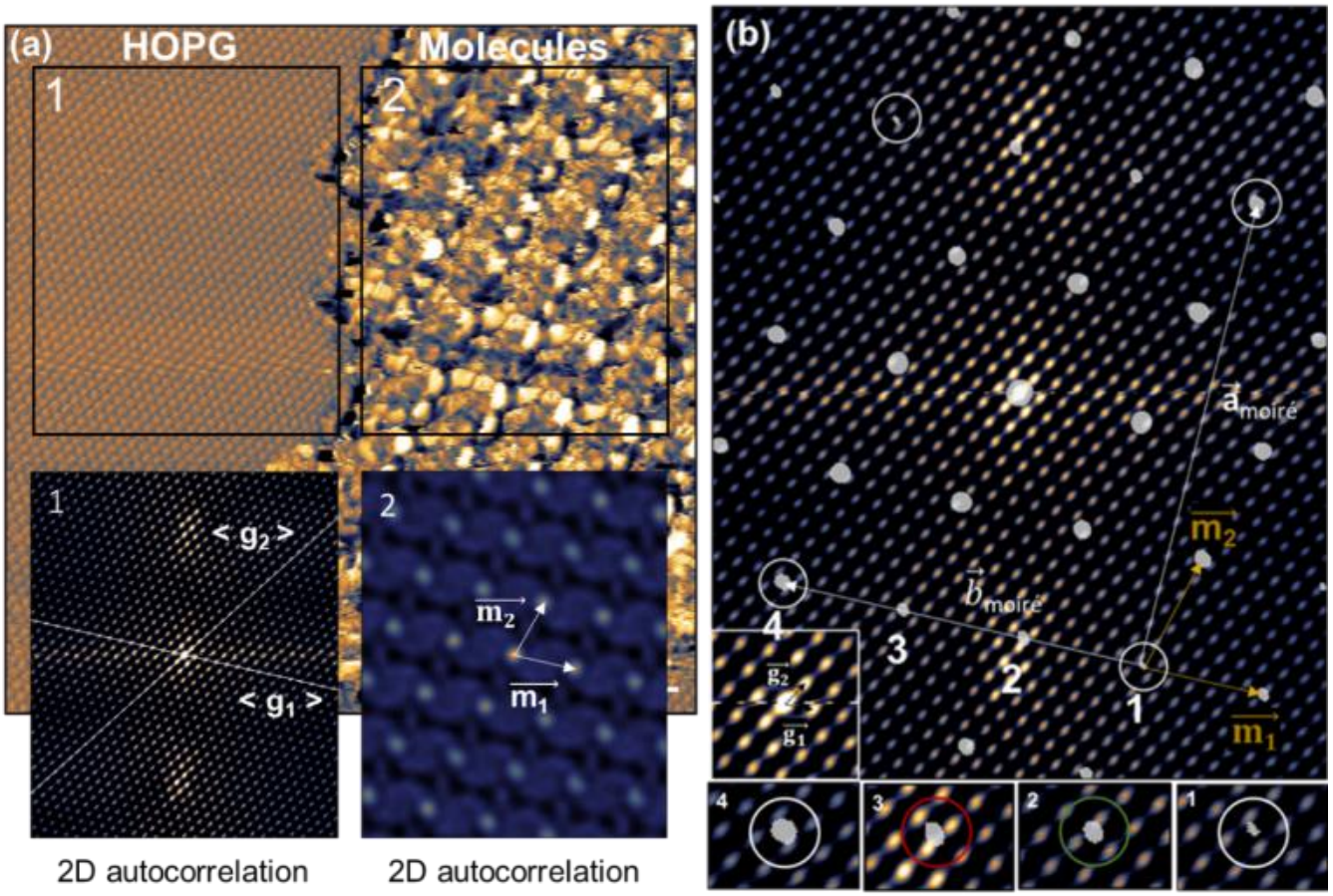

Figure 2. 2D autocorrelation treatment to extract the epitaxial relationship between the supramolecular phase and the HOPG surface. (a) STM image on the border between the HOPG and the supramolecular phase. It= 6 pA, Vs= 800 mV and of size 15 nm x 15 nm. Two areas of

this image, denoted 1 and 2, are cropped, and their 2D autocorrelation is calculated resulting in the two images below where lattice parameters can now be easily extracted. (b) The image resulting from the superposition of the two autocorrelation images extracted in (a). The molecular network nodes (white dots) are now clearly identifiable with respect to the HOPG network nodes (smaller yellow dots). In the lower part, a zoom of four successive molecular nodes in the $\mathbf{m_1}$ direction shows that nodes 1 and 4 have identical positions relative to the nodes of the HOPG. This identical molecular node position with respect to HOPG is found on other direction ($\mathbf{a_{moiré}}$) and is marked with a white circle.

By using the image in Figure 2a, we have developed a method that can relate the position of the center of each periodic motif of the molecular layer with respect to the HOPG network. This method consists first, in performing a 2D autocorrelation of two parts of this same image, one in the HOPG region and the other in the molecular region. Both parts have identical sizes and lie in the same horizontal band of the image, thus, undergoing the same thermal drift while imaging. Then, the contrast maxima are marked by threshold, and their positions are extracted. It is to be noted that these positions are those of the centers of each motif's features. The superposition of the extracted periodic molecular motif positions and the HOPG autocorrelation image give the illustration in Figure 2b. In this figure, we can identify several molecular nodes whose positions relative to the HOPG nodes are identical: for instance, nodes 1 and 4 in the insets in Figure 2b. The relative position corresponding to the nodes 1 compared to HOPG is found on the nodes 4 after a translation of vector $-3\mathbf{m_1}$ ($\mathbf{b_{moiré}}$). It is also found after a vector translation of $4\mathbf{m_2}-\mathbf{m_1}$ in the $\mathbf{a_{moiré}}$ direction. As we periodically find equivalent positions of the molecular nodes in two dimensions, we can express the correlation matrix with integer coefficients in eq 3 and show that the molecular layer assembles according to a 2D HOC phase on HOPG.

$$\begin{pmatrix} a_{\text{moiré}} \\ b_{\text{moiré}} \end{pmatrix} = \begin{pmatrix} -1 & 4 \\ -3 & 0 \end{pmatrix} \begin{pmatrix} m_1 \\ m_2 \end{pmatrix} = \begin{pmatrix} -14 & 27 \\ -17 & 0 \end{pmatrix} \begin{pmatrix} g_1 \\ g_2 \end{pmatrix} \quad (3)$$

The periodicity of bright line of Figure 1c can now be interpreted as a consequence of this HOC phase on the resulting STM contrast. The number '4' in the correlation matrix linked to $\mathbf{m_2}$ matches with the four motifs separation between the bright lines. It means that the distance between two successive bright lines can be reached after 4 $\mathbf{m_2}$ translation. We can reasonably associate the molecules located at the nodes of the Moiré pattern with a particular STM contrast (brighter in our case) and therefore this contrast will contribute to the formation of the bright line. However, in the $\mathbf{b_{moiré}}$ direction, no periodic modulation of the STM contrast is distinguished, but a study of the height profiles makes it possible to detect a periodicity after three molecular motifs in the $\mathbf{b_{moiré}}$ direction (see Figure S3). These results are confirmed by the fact that we found three identical molecular domains, rotated by 60° with respect to each other in accordance with the HOPG symmetry. By using eq. 3, we find the following theoretical values of the molecular lattice vectors m_1=1.39 nm and m_2=1.47 nm with an angle θ=77.34°. Taking the average of real space measurement on three STM images gives the experimental values $m_{1\text{-exp}}=1.56 \pm 0.2$ nm and $m_{2\text{-exp}}=1.46 \pm 0.2$ nm that makes and angle of $\theta_{exp}=77.09 \pm 1°$. Calibration coefficients $\alpha_{m_1}=m_{1\text{-exp}}/m_1$ and $\alpha_{m_2}=m_{2\text{-exp}}/m_2$ are deduced to be equal to 1.12 and 0.99 respectively.

It is important to keep in mind that the spots of maximum contrast in the autocorrelation image of the molecular phase do not mark the positions of the molecules but the positions of the smallest molecular periodic motif. This motif is composed of a dimer of molecules as illustrated in the inset of Figure 1c. The high-resolution STM image of Figure 1d allow us to determine relative distance between molecular dimer and molecule-molecule distance inside a dimer. These distances provide

information about the nature of inter-molecular interactions and allow us to suggest an adsorption model guided by NH···O hydrogen bonds for the supramolecular phase.

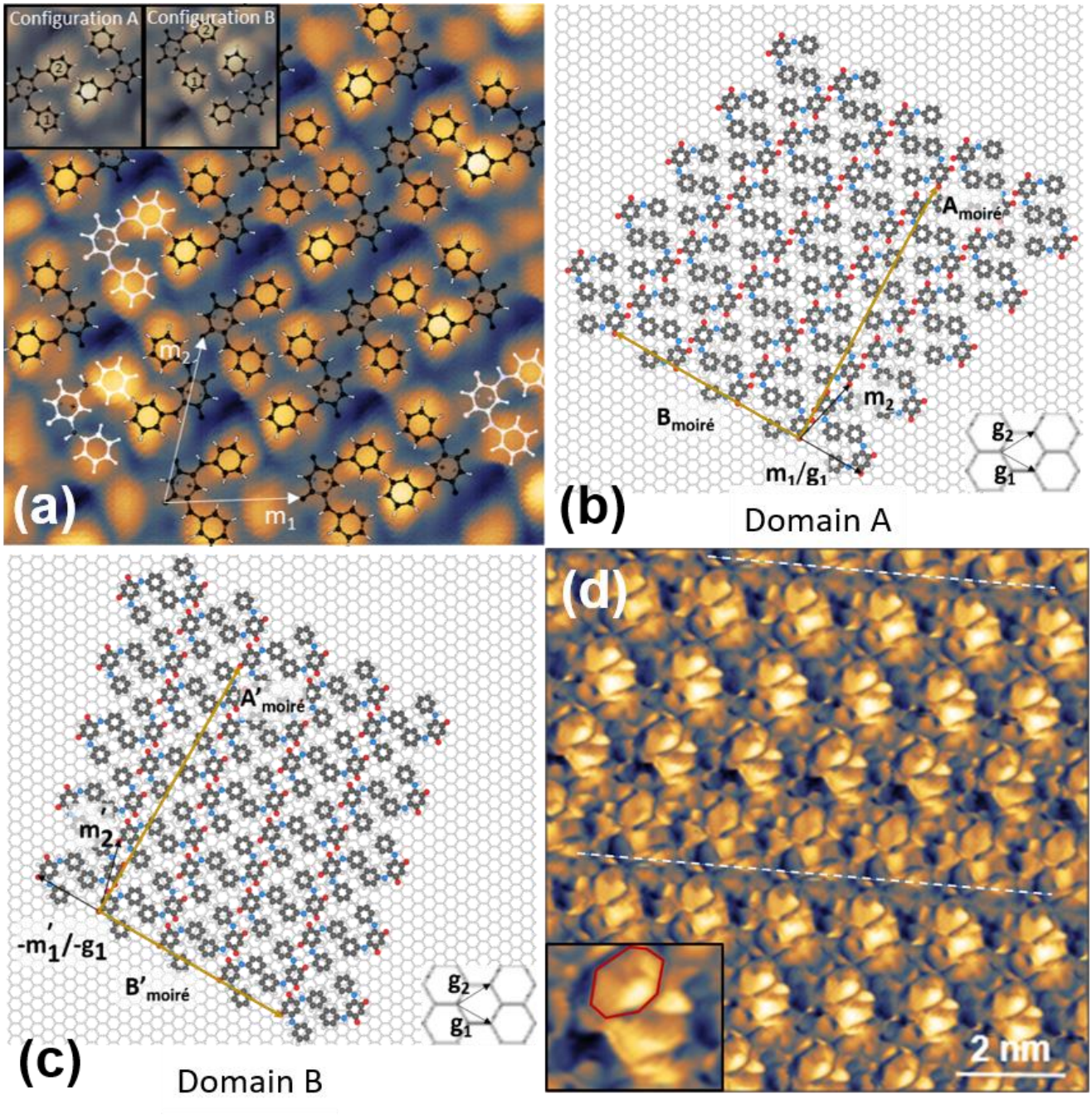

Figure 3. (a) High-resolution STM image highlighting the presence of a domain border (black line), characterized by a shift in the position of the molecules with respect to each other. The numbering of the phenyl rings accentuates this shift. In the molecular domain, the arrangement configuration A is characterized by a dimer with the phenyl ring '2' of the left molecule in between

two phenyl rings of the right molecule, meanwhile the opposite configuration B happens on the domain border with a phenyl ring '1' of the right molecule between two phenyl rings of the left molecule. The image was recorded at a tunneling current of It= 2 pA and sample voltage of Vs= -1.7 V. (b) Suggested ball and stick model of the domain A with molecules assumed to be rigid and lying flat on the surface. This model makes use of the derived correlation matrix coefficients in eq. 3 and assumes a random position of the first dimer of molecules. The HOPG, molecular, and moiré lattice vectors are highlighted on the image. (c) Suggested ball and stick model of the mirror domain B with molecules. (d) High-resolution STM image obtained with a functionalized tip. White dashed lines highlight the moiré, having a different contrast. In the inset, the molecular motif, with a hexagonal-like shaped feature whose dimensions are compatible with a phenyl ring. This suggests a rotation of the phenyl rings out of the plane of the surface. The image was recorded at a tunneling current of It= 4 pA and sample voltage of Vs= -320 mV.

The high-resolution STM image in Figure 3a highlights the presence of a domain border, which displays a shift in the position of the molecules comprised in the motif. If we name the phenyl rings of one DPQZ molecule of the dimer by '1' and '2' for the left and right rings respectively, we can presume the presence of two configurations A and B (inset in Figure 3a). The configuration A, which is mostly observed, is characterized by the phenyl ring '1' positioned in between two phenyl rings of the second molecule of the dimer (to the right). At some point, a new configuration B emerges, and is characterized by conversely the phenyl ring '2' positioned in between two phenyl rings of the second molecule of the dimer, the configuration A follows next, and the domain borders consist of the translation of half-a-molecule following $\mathbf{m}_2$. A and B configurations are symmetrical with respect to $\mathbf{m}_2$ and equivalent, so they will give rise to two mirror domains A and B. For example, in figure SI-2, we see a succession of close border domain. By making use of the

obtained values of the correlation matrix, we can construct a simple ball and stick model of the arrangement, shown in Figure 3(b-c), in which the molecules are assumed to be rigid and flat lying on the surface and the position of the first dimer of molecules is randomly chosen. Finally, since we have 3 possible orientations of the domains (rotated by 60° relative to each other) and that for each orientation, it is possible to have a mirror domain, this leads to 3x2 domain variants.

Figure 3d shows a high-resolution STM image of the same molecular layer phase obtained with a functionalized tip by an unknown cluster at the apex. The moiré lines of different contrast are highlighted with white dashed lines. The intramolecular resolution in the image clearly shows that the molecular motif encloses a hexagonal-like shaped feature (highlighted in red in the inset), whose dimensions are compatible with the dimensions of a phenyl ring. This feature suggests a rotation of the phenyl rings out of the surface plane. Steric hindrance and repulsive effects must also be considered, which complicates the prediction of the exact arrangement of the molecules on HOPG.

The results of Figure 3 allow to interpret the growth behavior of the 2D organic layer. In the Figure 1, we observe an anisotropic growth of the DPQZ molecules; a large domain extension following $\mathbf{m_2}$ with distances exceeding the micrometer, and smaller distances of the order of ten nanometers following $\mathbf{m_1}$. We can interpret this anisotropy as a response to the asymmetry of energy and directionality of the intermolecular interaction between the directions $\mathbf{m_1}$ and $\mathbf{m_2}$. In the direction $\mathbf{m_1}$, the interaction is related to a phenyl-phenyl interaction with two possible equivalent structural configurations (the two mirror domains A and B, see Figure 3) between successive molecules, resulting in frequent domain walls depending on which of these configurations is preferred. On the contrary, in the $\mathbf{m_2}$ direction, a much stronger and directive hydrogen-bond type interaction develops between two successive molecules without equivalent

structural configuration, stabilizing the growth over extended distances into a single direction. This interpretation, as well as its implication on the growth will be further discussed below using the results of the structure calculations.

1.2 DPQZ assembly on Graphene

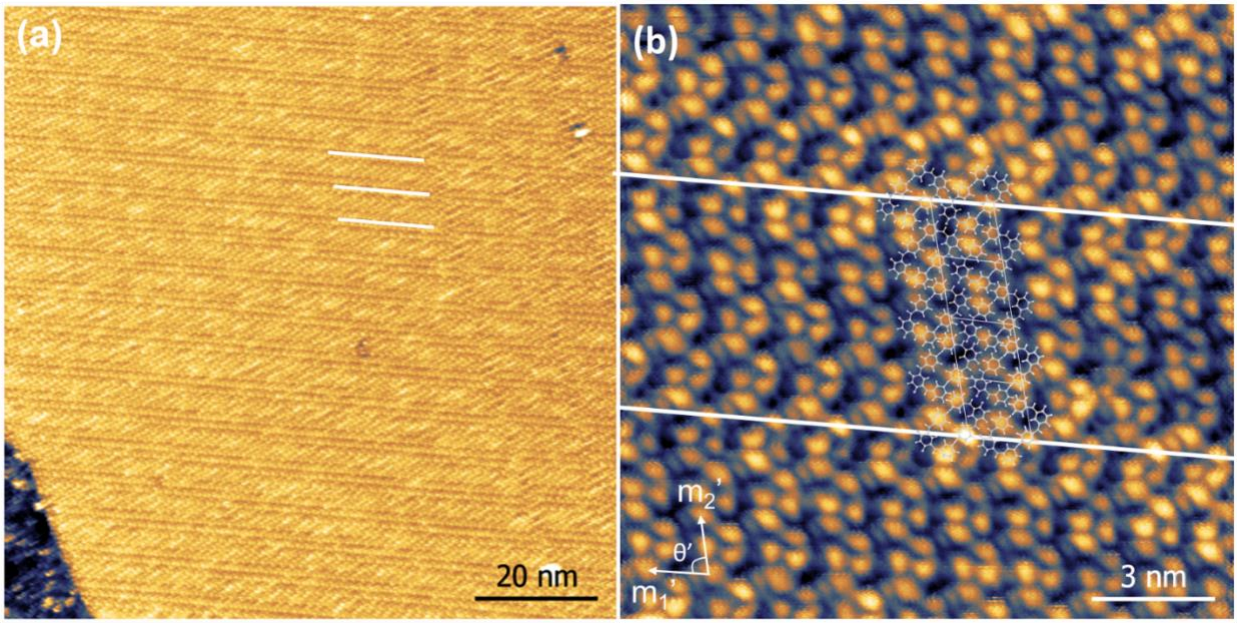

Figure 4: (a) STM image of the DPQZ molecules on graphene, white lines highlight the moiré. The image was recorded at a tunneling current of I_t= 2 pA, and a sample voltage V_s= 1.5 V. (b) STM image of a monolayer of DPQZ molecules on graphene surface with the moiré lines highlighted by white lines. Between two moiré lines, four molecular motifs are highlighted by white parallelograms. The image was recorded at a tunneling current of I_t= 2 pA and sample voltage of V_s= 0.3 V.

DPQZ molecules were deposited on graphene cooled down to -140 °C to ensure the growth of a supramolecular lattice comparable to the HOPG case using the same molecular flux as in the DPQZ/HOPG case.

The Figure 4a shows a medium scale image of the self-assembled ML resulting from the adsorption of the DPQZ molecules on the graphene substrate. Periodic lines of different contrast, assumed to be related to a moiré effect, are observed and highlighted with white lines. On the high-resolution STM image in Figure 4b we see that we can identify four repeating units between two moiré lines; molecular motifs that enclose features similar to the ones observed on HOPG. We measure the molecular lattice constants to be $m'_{1\text{-exp}}=1.54 \pm 0.10$ nm and $m'_{2\text{-exp}}=1.44 \pm 0.16$ nm and an angle of 76.1°. These measurements are the average real-space measurements taken from nine images, where the uncertainty is based on the difference between the highest and lowest values measured. By applying the calibration coefficients α_{m1} and α_{m2} calculated in the previous subsection, we can correct these values to get m_1'=1.37 nm and m_2'=1.45 nm. These values are in very good agreement with the ones obtained for DPQZ /HOPG.

The similar moiré effect and motif features, in terms of dimensions and angles, show that the self-assembly on graphene is structurally identical to the one on HOPG. The findings from earlier publications reveal that HOPG can serve as a model surface for graphene [10–13], and our conclusions regarding the growth mode of the layer on HOPG and the supramolecular phase apply also to DPQZ on graphene/SiC.

To confirm the anisotropic growth interpretation and to explore the possibility for this supramolecular network to induce a periodic surface potential modulation, it is needed to simulate the different interaction energies, and the resulting dipole at the few-molecules scale.

1.2 Computational results

Computational chemistry calculations were performed to get insights into the 2D self-assembly structure of DPQZ molecules on the graphene surface and interaction nature. The most stable stacked pattern was found from all possible packing arrangements of DPQZ molecules in all reasonable space groups. Consequently, DPQZ molecules must self-organize on the graphene surface *via* stacked patterns of C_2 symmetry, where two main interactions influence the molecular orientation on graphene, i.e., i) chains of hydrogen-bonded molecules involving the O and N–H groups, and ii) bonding with neighboring molecules via CH···HC interactions between phenyl rings (Figure 5a). The latter agrees with the suggested ball and stick model with molecules assumed rigid and lying flat on the surface, in addition to the high-resolution STM images in Figures 3(a-b). Note that free DPQZ molecules show a torsion angle of ~34° between rings, decreasing below 13° when adsorbed onto graphene. Accordingly, monolayers of DPQZ molecules lie almost flat at intermolecular distances of ~3.3 Å from graphene; the separation between adsorbates is in the range of 2.0-2.3 Å (Figure 5b), denoting the strong influence of intermolecular driving forces in the 2D self-assemblies.

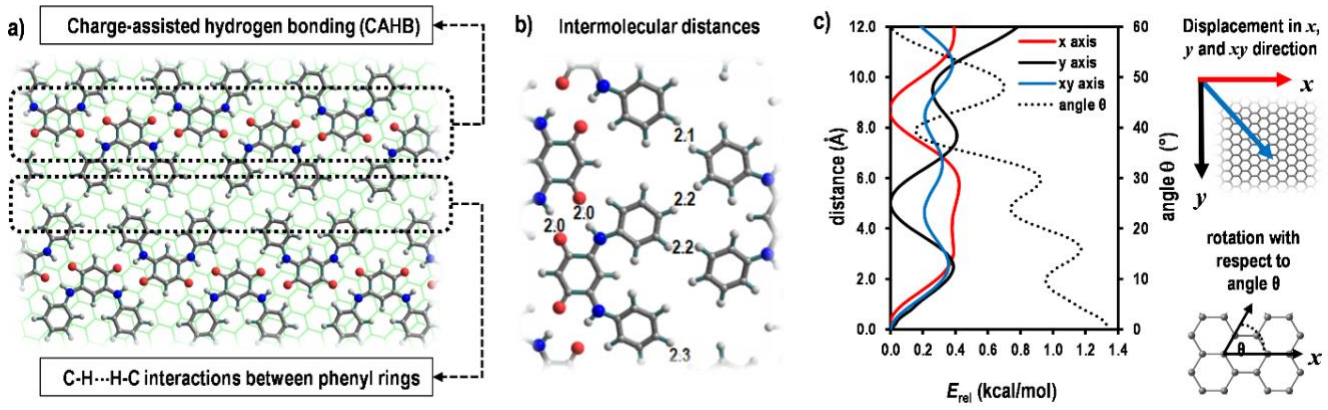

Figure 5. (a). Computed adsorption pattern of the 2D self-assembly on graphene. (b). Intermolecular distances (in Å) between dimers on the 2D self-assembly. (c) Relative energy (E_{rel}, in kcal/mol) with respect to the ground state. Displacements of the 2D self-assembly along the *x*, *y* and *xy* direction of graphene. Rotation of the 2D self-assembly occurs with respect to the angle θ formed in benzene type rings of graphene.

Figure 5c shows the potential energy surface resulting from the translation and rotation of the 2D self-assembly with respect to the graphene surface. Accordingly, new energy minima are reached with translations of 8.4 Å in the x direction which correspond to two periods in this direction, and 4.9 Å in *y* direction which correspond to two periods in this direction. In addition, metastable states can be reached by translation movements on the graphene surface, which are obtained by bypassing energy barriers of up to 0.4 kcal/mol (~0.02 eV). These metastable states correspond to arrangements with higher energies than the ground state that can be reached with low energy barriers. In fact, translations in the *xy* direction result only in metastable states due to the high lattice periodicity. Furthermore, the rotation with respect to the graphene surface is also allowed, showing low energy barriers between the metastable states (up to 1.2 kcal/mol). The weak energy barriers suggest that translations and rotations of the 2D self-assembly on the graphene surface are allowed, and the existence of metastable geometries would stabilize these movements. These results are in accordance with the presence of different domain rotated by 60°.

Regarding the stability of the 2D self-assembled structure, the binding energy is estimated at ~1.94 eV per DPQZ molecule, which is comparable to the binding energy of *p*-benzoquinonemonoimine zwitterion on Cu(111) surfaces (1.9 eV).[15] Dispersion-corrected DFT calculations at the PBE-D3/def2-SVP level were also performed to analyze the graphene-DPQZ interface based on a finite cluster model containing a single dimer interaction. In the first place,

the chains of hydrogen bonded DPQZ molecules bind together (independently of the graphene surface) with binding energies of 0.8 eV per dimer, where the stabilizing energy is ~64% due to electrostatic driving forces as obtained from EDA calculations (Figure 6a); the latter is consistent with the formation of charge assisted hydrogen bonds (CAHB) between dimers because the binding energy is larger than typical hydrogen bonds. Otherwise, the bonding with neighboring DPQZ molecules *via* CH···HC interactions take place with lower binding energies of ~0.1 eV per molecule, which is almost entirely due to dispersion effects (70%) (Figure 6a). Then, the stability of the self-assembled DPQZ structure is enhanced by the formation of intermolecular CAHBs between dimers and the dispersion attraction of neighboring molecules. This energy difference between these two intermolecular bonding (a pretty strong CAHB and a relatively weak CH···HC bonding) which have different direction is at the origin of the anisotropic behavior of the molecular growth.

In the case of the graphene-DPQZ interface (Figure 6b), the adsorption of each DPQZ dimer on graphene is strongly influenced by the interplay between dispersion (53%) and electrostatics effects (42%), denoting that a balance between long-range driving forces is responsible for the high stability of the self-assembly. IGMH analysis shows that dispersion interactions emerge from the π-π stacking between phenyl rings of DPQZ and benzene type rings of graphene surface (green regions in Figure 6b). ALMO-EDA results show that the π-π stacking stand for 4.9 eV of the stabilizing dispersion energy gained per adsorbed dimer. The electrostatic part emerges from the interaction between activated carbon atoms of graphene and the charged C, O, and N atoms in the zwitterion molecules, standing for 3.8 eV of the stabilizing energy gained per adsorbed dimer (green regions in Figure 6b). It is important to note that the π-π stacking introduces steric effects in the adsorption process due to Pauli repulsion (volume exclusion effects

when molecular fragments are sufficiently close), which stand for 6.6 eV of the destabilizing energy (red regions in Figure 6b). Nevertheless, the stability gained by electrostatics/dispersion effects is high enough to overcompensate the Pauli repulsion, leading to stable self-assemblies ($|\Delta E_{dispersion}+\Delta E_{electrostatics}|>\Delta E_{Pauli}$).

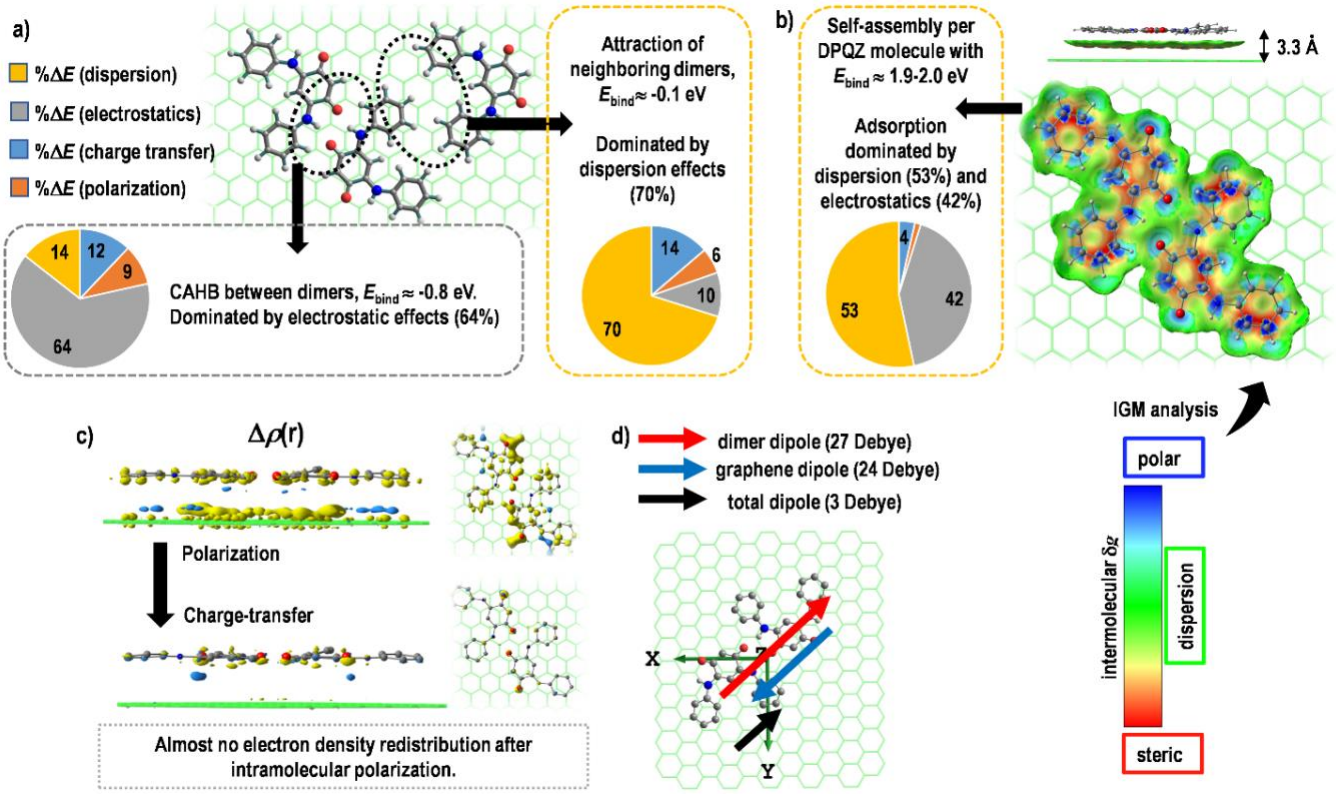

Figure 6. (a) Intermolecular interactions between dimers and ALMO-EDA analysis of driving forces. (b) Intermolecular interactions between dimers and graphene, with the quantitative/qualitative ALMO-EDA and IGM results of intermolecular interactions. (c) Electron density difference [Δρ(r)] on local domains of the graphene-DPQZ interface and due to charge rearrangements resulting from polarization and charge-transfer effects. (d) Fragmental dipole moment analysis on local domains of the graphene-DPQZ interface.

Additionally, the short-range stabilizing effects, i.e., charge transfer and polarization, have minor contributions to the stabilizing energy, with a combined contribution of 5% per adsorbed dimer; the latter is reasonable with the lack of orbital overlapping. Nevertheless, the graphene surface shows a mild reorganization of the electron density upon adsorption. Figure 6c displays the electron density difference [$\Delta\rho$(r)] due to the charge reorganization reached by polarization and charge transfer. Graphene and DPQZ systems mutually polarize at 3.3 Å, resulting in the on-fragment density relaxation of each fragment to their electrons/nuclei; the latter triggers induced multipole moments on the fragments. Most of the charge rearrangements in the graphene-DPQZ interface occurs at the polarization step, accumulating electrons at intramolecular regions with an energy lowering of 0.12 eV per dimer. Subsequently, the virtual and occupied orbitals can be mixed after polarization, but the lack of orbital overlapping leads to weak electron transfer in the graphene→ DPQZ direction (~0.05 *e* per molecule); the gained electron density is allocated near to 2*p* orbitals of oxygen atoms in the DPQZ dimers, which stand for energy lowering of ~0.32 eV per adsorbed dimer. The electron density rearrangements will be responsible for i) the enhancement of the intermolecular electrostatic attraction (considering that graphene is non-polar before interaction) and ii) characteristics of the resulting dipole upon adsorption. In this regard, the free DPQZ molecules show computed dipoles of 9.6 Debye, which change to almost 0 in dimers because the dipoles are aligned in opposite directions, while the graphene surface is non-polarized. Upon adsorption, the electron density rearrangements cause induced dipoles on the graphene surface and adsorbed dimers, where the dipole vectors are aligned with the surface plane (Figure 6d). The fragmental dipoles on the graphene and DPQZ dimers have different magnitudes of 23.8 and 27.2 Debye, respectively, but are aligned in opposite directions. Consequently, the

interface shows local dipoles aligned with the graphene surface plane (~3.4 Debye per adsorbed dimer).

The computational chemistry calculations carried out in this part made it possible to explain the growth mechanism on the 2D self-assembly structure of DPQZ molecules on graphene surfaces by giving the energetic order of magnitude of the intermolecular interaction and the molecule-substrate interaction and their physical origin. It was determined that DPQZ molecules tend to organize themselves on graphene surfaces through stacked patterns of C2 symmetry, influenced by hydrogen bonding and CH···HC interactions between phenyl rings, according to experimental result. The orientation of the molecules becomes nearly flat upon adsorption onto graphene, with a significant decrease in the torsion angle between rings, indicating strong intermolecular driving forces. The study further explored the potential energy landscape of the self-assembly, revealing translations and rotations as allowed movements with weak energy barriers, which, in addition to the symmetry of the substrate, explains the presence of domains rotated at 60° from each other. Detailed analysis of the graphene-DPQZ interface highlighted the interplay between dispersion and electrostatic effects, with both playing crucial roles in the stability of the self-assembly. Intermolecular π-π stacking between phenyl rings of DPQZ and benzene rings of the graphene surface contributed significantly to dispersion interactions, while electrostatic interactions stemmed from the interaction between activated carbon atoms of graphene and charged atoms in DPQZ molecules. Despite steric effects introduced by π-π stacking, the stability gained from dispersion and electrostatic effects outweighed destabilizing factors, resulting in stable self-assemblies. Furthermore, the study elucidated the charge reorganization and polarization effects occurring at the graphene-DPQZ interface, leading to induced dipoles aligned with the graphene surface plane.

Conclusions

By carefully analyzing the high-resolution STM images, we have found that the DPQZ molecules physisorb in a head to tail self-assembled dimer configuration on HOPG as well as on graphene, with a visible moiré effect. The study of the epitaxial relationship between the molecule lattice and HOPG lattice indicates that the origin of this visible moiré effect is due to the high order commensurability between the two layers. ALMO-EDA analyses confirm that the self-assembled DPQZ structure is stabilized by the formation of intermolecular CAHBs between dimers and by the dispersion attraction between the phenyl rings of neighboring molecules. The strong difference of these interactions in terms of directionality, binding energy and equivalent linking fully explain the anisotropic growth of the molecular layer. Although the dipole resulting from a molecular dimer vanishes, the redistribution of the electron density of graphene caused by the adsorption of this dimer breaks the symmetry of the resulting dipole and generates localized dipoles at the interface of approximately 3.4 Debye per dimer. These local dipoles meet one of the requirements for the modulation of the electrostatic surface potential and the engineering of the band structure of graphene. As a perspective for future work, it would be possible to measure at the molecular scale the local modulation of this surface potential with Kelvin spectroscopy as well as the modifications of electronic density induced by the layer of molecules.

AUTHOR INFORMATION

Corresponding Author

E-mail thomas.leoni@univ-amu.fr

Present Addresses

Simon Pascal † CEISAM - UMR 6230 CNRS Nantes Université 2 rue de la Houssinière, BP 92208 44322 Nantes Cedex 3.

Author Contributions

The experiment was conceived by T.L. The STM measurements was performed and analyzed by G.N, T.L, A.R, L.M., C.B., and R.P.. S.P., G.C., O.S., and G.N. synthesized the molecule. D.CA., and L.SV. performed the computational chemistry calculations. H.H., P.L., M.P., and S.C. synthesized the graphene sample. The manuscript was written through contributions of all authors. All authors have given approval to the final version of the manuscript.

Acknowledgment

We thanks the ANR agency thought the project ANR-22-CE09-0020-SUPERZIC

D.C-A thanks to ANID/FONDECYT 1210355 and ANID/FONDEQUIP EQM180180.

SUPPORTING INFORMATION

Additional experimental details and measurements on STM images in S1-S3, and additional computational results in S4-S7 as mentioned in the text.

ABBREVIATIONS

2D	Two-dimensional
vdW	Van der Waals
h-vdWH	Hybrid van der Waals Heterostructures
HOPG	Highly Oriented Pyrolytic Graphite
UHV	Ultra High Vacuum
DPQZ	Di-Phenyl functionalized *p*-benzoQuinonemonoimine Zwitterion
STM	Scanning Tunneling Microscopy
LT-STM/AFM	Low Temperature-Scanning Tunneling Microscopy/Atomic Force Microscopy
1D-FFT	One-dimensional-Fast Fourier Transform
HOC	High Order Commensurate
LEED	Low Energy Electron Diffraction

REFERENCES

(1) Gobbi, M.; Orgiu, E.; Samorì, P. When 2D Materials Meet Molecules: Opportunities and Challenges of Hybrid Organic/Inorganic van Der Waals Heterostructures. *Adv. Mater.* **2018**, *30* (18), 1706103. https://doi.org/10.1002/adma.201706103.

(2) Jariwala, D.; Howell, S. L.; Chen, K.-S.; Kang, J.; Sangwan, V. K.; Filippone, S. A.; Turrisi, R.; Marks, T. J.; Lauhon, L. J.; Hersam, M. C. Hybrid, Gate-Tunable, van Der Waals p–n Heterojunctions from Pentacene and MoS_2. *Nano Lett.* **2016**, *16* (1), 497–503. https://doi.org/10.1021/acs.nanolett.5b04141.

(3) Kim, B. J.; Hwang, E.; Kang, M. S.; Cho, J. H. Electrolyte-Gated Graphene Schottky Barrier Transistors. *Adv. Mater.* **2015**, *27* (39), 5875–5881. https://doi.org/10.1002/adma.201502020.

(4) Boulet, I.; Pascal, S.; Bedu, F.; Ozerov, I.; Ranguis, A.; Leoni, T.; Becker, C.; Masson, L.; Matkovic, A. et al. Electrical Monitoring of Organic Crystal Phase Transition Using MoS_2 Field Effect Transistor. *Nanoscale Adv.* **2023**, *5* (6), 1681–1690. https://doi.org/10.1039/D2NA00817C.

(5) Kiriya, D.; Tosun, M.; Zhao, P.; Kang, J. S.; Javey, A. Air-Stable Surface Charge Transfer Doping of MoS_2 by Benzyl Viologen. *J. Am. Chem. Soc.* **2014**, *136* (22), 7853–7856. https://doi.org/10.1021/ja5033327.

(6) Park, C.-H.; Yang, L.; Son, Y.-W.; Cohen, M. L.; Louie, S. G. New Generation of Massless Dirac Fermions in Graphene under External Periodic Potentials. *Phys. Rev. Lett.* **2008**, *101* (12), 126804. https://doi.org/10.1103/PhysRevLett.101.126804.

(7) Cao, Y.; Fatemi, V.; Fang, S.; Watanabe, K.; Taniguchi, T.; Kaxiras, E.; Jarillo-Herrero, P. Unconventional Superconductivity in Magic-Angle Graphene Superlattices. *Nature* **2018**, *556* (7699), 43–50. https://doi.org/10.1038/nature26160.

(8) Bistritzer, R.; MacDonald, A. H. Moiré Bands in Twisted Double-Layer Graphene. *Proc. Natl. Acad. Sci.* **2011**, *108* (30), 12233–12237. https://doi.org/10.1073/pnas.1108174108.
(9) Gobbi, M.; Bonacchi, S.; Lian, J. X.; Liu, Y.; Wang, X.-Y.; Stoeckel, M.-A.; Squillaci, M. A.; D'Avino, G.; Narita, A.; Müllen, K. et al. Periodic Potentials in Hybrid van Der Waals Heterostructures Formed by Supramolecular Lattices on Graphene. *Nat. Commun.* **2017**, *8* (1), 14767. https://doi.org/10.1038/ncomms14767.
(10) Le Liepvre, S.; Du, P.; Kreher, D.; Mathevet, F.; Attias, A.-J.; Fiorini-Debuisschert, C.; Douillard, L.; Charra, F. Fluorescent Self-Assembled Molecular Monolayer on Graphene. *ACS Photonics* **2016**, *3* (12), 2291–2296. https://doi.org/10.1021/acsphotonics.6b00793.
(11) Li, B.; Tahara, K.; Adisoejoso, J.; Vanderlinden, W.; Mali, K. S.; De Gendt, S.; Tobe, Y.; De Feyter, S. Self-Assembled Air-Stable Supramolecular Porous Networks on Graphene. *ACS Nano* **2013**, *7* (12), 10764–10772. https://doi.org/10.1021/nn4039047.
(12) Du, P.; Jaouen, M.; Bocheux, A.; Bourgogne, C.; Han, Z.; Bouchiat, V.; Kreher, D.; Mathevet, F.; Fiorini-Debuisschert, C.; Charra, F. et al. Surface-Confined Self-Assembled Janus Tectons: A Versatile Platform towards the Noncovalent Functionalization of Graphene. *Angew. Chem. Int. Ed.* **2014**, *53* (38), 10060–10066. https://doi.org/10.1002/anie.201403572.
(13) MacLeod, J. M.; Lipton-Duffin, J. A.; Cui, D.; De Feyter, S.; Rosei, F. Substrate Effects in the Supramolecular Assembly of 1,3,5-Benzene Tricarboxylic Acid on Graphite and Graphene. *Langmuir* **2015**, *31* (25), 7016–7024. https://doi.org/10.1021/la5048886.
(14) Dowben, P. A.; Kunkel, D. A.; Enders, A.; Rosa, L. G.; Routaboul, L.; Doudin, B.; Braunstein, P. The Dipole Mediated Surface Chemistry of P-Benzoquinonemonoimine Zwitterions. *Top. Catal.* **2013**, *56* (12), 1096–1103. https://doi.org/10.1007/s11244-013-0075-5.
(15) Kunkel, D. A.; Simpson, S.; Nitz, J.; Rojas, G. A.; Zurek, E.; Routaboul, L.; Doudin, B.; Braunstein, P.; Dowben, P. A.; Enders, A. Dipole Driven Bonding Schemes of Quinonoid Zwitterions on Surfaces. *Chem. Commun.* **2012**, *48* (57), 7143–7145. https://doi.org/10.1039/C2CC32462H**.**
(16) Fang, Y.; Nguyen, P.; Ivasenko, O.; Aviles, M. P.; Kebede, E.; Askari, M. S.; Ottenwaelder, X.; Ziener, U.; Siri, O.; Cuccia, L. A. Charge-Assisted Hydrogen Bond-Directed Self-Assembly of an Amphiphilic Zwitterionic Quinonemonoimine at the Liquid–Solid Interface. *Chem. Commun.* **2011**, *47* (40), 11255. https://doi.org/10.1039/c1cc14085j.
(17) Tamboura, F. B.; Cazin, C. S. J.; Pattacini, R.; Braunstein, P. Reactions of Amines with Zwitterionic Quinoneimines: Synthesis of New Anionic and Zwitterionic Quinonoids. *Eur. J. Org. Chem.* **2009**, *2009* (20), 3340–3350. https://doi.org/10.1002/ejoc.200900154.
(18) Siri, O.; Braunstein, P. Unprecedented Zwitterion in Quinonoid Chemistry. *Chem. Commun.* **2002**. https://doi.org/10.1039/b107828n.
(19) Landois, P.; Wang, T.; Nachawaty, A.; Bayle, M.; Decams, J.-M.; Desrat, W.; Zahab, A.-A.; Jouault, B.; Paillet, M.; Contreras, S. Growth of Low Doped Monolayer Graphene on SiC(0001) via Sublimation at Low Argon Pressure. *Phys. Chem. Chem. Phys.* **2017**, *19* (24), 15833–15841. https://doi.org/10.1039/C7CP01012E.
(20) Wang, T.; Huntzinger, J.-R.; Bayle, M.; Roblin, C.; Decams, J.-M.; Zahab, A.-A.; Contreras, S.; Paillet, M.; Landois, P. Buffer Layers Inhomogeneity and Coupling with Epitaxial Graphene Unravelled by Raman Scattering and Graphene Peeling. *Carbon* **2020**, *163*, 224–233. https://doi.org/10.1016/j.carbon.2020.03.027.

(21) *Gwyddion: an open-source software for SPM data analysis*. https://www-degruyter-com.lama.univ-amu.fr/document/doi/10.2478/s11534-011-0096-2/html (accessed 2023-11-17).
(22) D.S. BIOVIA, Polymorph/Adsorption Locator, BIOVIA Materials Studio 2022, Version 22.1.0.3462, San Diego: Dassault Systèmes, 2022.
(23) *GFN2-xTB—An Accurate and Broadly Parametrized Self-Consistent Tight-Binding Quantum Chemical Method with Multipole Electrostatics and Density-Dependent Dispersion Contributions | Journal of Chemical Theory and Computation*. https://pubs-acs-org.lama.univ-amu.fr/doi/10.1021/acs.jctc.8b01176 (accessed 2023-11-17).
(24) Perdew, J. P.; Burke, K.; Wang, Y. Generalized Gradient Approximation for the Exchange-Correlation Hole of a Many-Electron System. *Phys. Rev. B* **1996**, *54* (23), 16533–16539. https://doi.org/10.1103/PhysRevB.54.16533.
(25) Weigend, F.; Ahlrichs, R. Balanced Basis Sets of Split Valence, Triple Zeta Valence and Quadruple Zeta Valence Quality for H to Rn: Design and Assessment of Accuracy. *Phys. Chem. Chem. Phys.* **2005**, *7* (18), 3297–3305. https://doi.org/10.1039/B508541A.
(26) Grimme, S.; Antony, J.; Ehrlich, S.; Krieg, H. A Consistent and Accurate Ab Initio Parametrization of Density Functional Dispersion Correction (DFT-D) for the 94 Elements H-Pu. *J. Chem. Phys.* **2010**, *132* (15), 154104. https://doi.org/10.1063/1.3382344.
(27) Grimme, S.; Ehrlich, S.; Goerigk, L. Effect of the Damping Function in Dispersion Corrected Density Functional Theory. *J. Comput. Chem.* **2011**, *32* (7), 1456–1465. https://doi.org/10.1002/jcc.21759.
(28) Horn, P. R.; Mao, Y.; Head-Gordon, M. Probing Non-Covalent Interactions with a Second Generation Energy Decomposition Analysis Using Absolutely Localized Molecular Orbitals. *Phys. Chem. Chem. Phys.* **2016**, *18* (33), 23067–23079. https://doi.org/10.1039/C6CP03784D.
(29) Horn, P. R.; Mao, Y.; Head-Gordon, M. Defining the Contributions of Permanent Electrostatics, Pauli Repulsion, and Dispersion in Density Functional Theory Calculations of Intermolecular Interaction Energies. *J. Chem. Phys.* **2016**, *144* (11), 114107. https://doi.org/10.1063/1.4942921.
(30) Shao, Y.; Gan, Z.; Epifanovsky, E.; Gilbert, A. T. B.; Wormit, M.; Kussmann, J.; Lange, A. W.; Behn, A.; Deng, J.; Feng, X. et al. Advances in Molecular Quantum Chemistry Contained in the Q-Chem 4 Program Package. *Mol. Phys.* **2015**, *113* (2), 184–215. https://doi.org/10.1080/00268976.2014.952696.
(31) Neese, F. Software Update: The ORCA Program System, Version 4.0. *WIREs Comput. Mol. Sci.* **2018**, *8* (1), e1327. https://doi.org/10.1002/wcms.1327.
(32) Lefebvre, C.; Rubez, G.; Khartabil, H.; Boisson, J.-C.; Contreras-García, J.; Hénon, E. Accurately Extracting the Signature of Intermolecular Interactions Present in the NCI Plot of the Reduced Density Gradient versus Electron Density. *Phys. Chem. Chem. Phys.* **2017**, *19* (27), 17928–17936. https://doi.org/10.1039/C7CP02110K.
(33) Lu, T.; Chen, F. Multiwfn: A Multifunctional Wavefunction Analyzer. *J. Comput. Chem.* **2012**, *33* (5), 580–592. https://doi.org/10.1002/jcc.22885.
(34) Tamboura, F. B.; Cazin, C. S. J.; Pattacini, R.; Braunstein, P. Reactions of Amines with Zwitterionic Quinoneimines: Synthesis of New Anionic and Zwitterionic Quinonoids. *Eur. J. Org. Chem.* **2009**, *2009* (20), 3340–3350. https://doi.org/10.1002/ejoc.200900154.
(35) Routaboul, L.; Braunstein, P.; Xiao, J.; Zhang, Z.; Dowben, P. A.; Dalmas, G.; Da Costa, V.; Félix, O.; Decher, G.; Rosa, L. G. et al. Altering the Static Dipole on Surfaces through

Chemistry: Molecular Films of Zwitterionic Quinonoids. *J. Am. Chem. Soc.* **2012**, *134* (20), 8494–8506. https://doi.org/10.1021/ja212104b.
(36) Simpson, S.; Kunkel, D. A.; Hooper, J.; Nitz, J.; Dowben, P. A.; Routaboul, L.; Braunstein, P.; Doudin, B.; Enders, A.; Zurek, E. Coverage-Dependent Interactions at the Organics–Metal Interface: Quinonoid Zwitterions on Au(111). *J. Phys. Chem. C* **2013**, *117* (32), 16406–16415. https://doi.org/10.1021/jp403384h.
(37) Yuan, M.; Tanabe, I.; Bernard-Schaaf, J.-M.; Shi, Q.-Y.; Schlegel, V.; Schurhammer, R.; Dowben, P. A.; Doudin, B.; Routaboul, L.; Braunstein, P. Influence of Steric Hindrance on the Molecular Packing and the Anchoring of Quinonoid Zwitterions on Gold Surfaces. *New J. Chem.* **2016**, *40* (7), 5782–5796. https://doi.org/10.1039/C5NJ03251B.
(38) Spitzer, S.; Helmle, O.; Ochs, O.; Horsley, J.; Martsinovich, N.; Heckl, W. M.; Lackinger, M. What Can Be Inferred from Moiré Patterns? A Case Study of Trimesic Acid Monolayers on Graphite. *Faraday Discuss.* **2017**, *204*, 331–348. https://doi.org/10.1039/C7FD00113D.

Table Of Contents

Author Contributions

Funding sources

ACKNOWLEDGMENT

ABBREVIATIONS

REFERENCES